Diffuse optics using a dual window fast-gated counter

Laura Di Sieno,[1] Alberto Dalla Mora,[1,*] Gianluca Boso,[2] Alberto Tosi,[2] Antonio Pifferi,[1,3] Rinaldo Cubeddu,[1,3] and Davide Contini[1]

[1]Dipartimento di Fisica, Politecnico di Milano, Piazza Leonardo da Vinci 32, 20133 Milano, Italy
[2]Dipartimento di Elettronica, Informazione e Bioingegneria, Politecnico di Milano, Piazza Leonardo da Vinci 32, 20133 Milano, Italy
[3]CNR, Istituto di Fotonica e Nanotecnologie, Piazza Leonardo da Vinci 32, 20133 Milano, Italy
*Corresponding author: alberto.dallamora@polimi.it

Received 16 July 2014; accepted 18 September 2014;
posted 24 September 2014; published 27 October 2014

1. Introduction

In the last decades light has become attractive as a noninvasive tool to investigate diffusive media [1]. In particular, great effort has been devoted in the development of systems exploiting time-resolved approaches to diffuse optics due to the different advantages provided by this technique. The most important one is its intrinsic capability of encoding depth information in time. Early-arriving photons are those that travelled only in the superficial layer of the medium while photons arriving later have visited deeper structures [2].

For this purpose, time-resolved diffuse optical spectroscopy (TR-DOS) is proposed in different clinical applications [3] such as brain monitoring [4,5], muscle oximetry [6], breast cancer detection [7–11], breast density assessment [12], monitoring neoadjuvant chemotherapy [13], and the study of osteoporosis [14]. In recent years, both industries and researchers have shown a rising interest in scaling TR-DOS setups in order to create low-cost, portable, and fully noninvasive devices for clinical diagnostics and monitoring (e.g., optical mammography and functional brain imaging).

Applications of TR-DOS extend also to nonmedical fields such as assessment of fruit quality [15], wood characterization [16], and analysis of pharmaceutical tablets [17]. Also in these cases, industries require compact and low-cost instruments.

Along the path toward compact and low-cost devices, the enormous growth in photonics components for light sources (e.g., compact-pulsed laser diodes) and detectors [e.g., single-photon avalanche diodes (SPAD)] meets this request of scaling both size and

cost, whereas the most challenging element to be scaled is the time-correlated single-photon counting (TCSPC) system.

In this paper we demonstrate the possibility to use a novel dual-window fast-gated counter (device architecture and basic performance assessment already presented in [18]) which has enhanced performances with respect to other commercially available gated counters [19–21]. It can be used as a simpler yet comparable solution with respect to a standard TCSPC setup. This equivalence is investigated also in the case of small source–detector distance (ρ) approaches [22]. Indeed, we have demonstrated that null-ρ provides better contrast, spatial resolution, and signal intensity as compared to large-ρ measurements in the case of time-resolved diffuse optical imaging in reflectance geometry, provided that an efficient gate is applied to extract the few late deep-travelling photons out of the burst of early-swallower photons [23].

In this work performances of the gated counter approach have been validated in different measurements: (i) contrast produced by a localized totally absorbing inclusion; (ii) absorption coefficient variation in bilayer structures; (iii) absorption coefficient estimation in homogeneous media; and (iv) *in vivo* arterial occlusion on healthy volunteer.

This paper is organized as follows: Section 2 deals with the experimental setup and data analysis; results and their discussion are shown in Section 3; finally, in Section 4 we summarize the work and discuss future perspectives.

2. Materials and Methods

A. Experimental Setup

The experimental setup is shown in Fig. 1. The light source is a pulsed laser prototype based on a four-wave mixing process at 710 nm wavelength, featuring 30 ps time duration pulses, 40 MHz repetition rate, and 120 mW maximum average power (Fianium Ltd, UK). Light exiting from the laser is properly attenuated by means of a variable optical attenuator and then injected into the sample through a 400 μm core optical fiber. Back-diffused photons are then collected at a given source–detector distance with a 1 mm core fiber and focused onto the photodetector. We use a reflectance geometry with different distances between source and detection fibers, depending on the aim of the experiment.

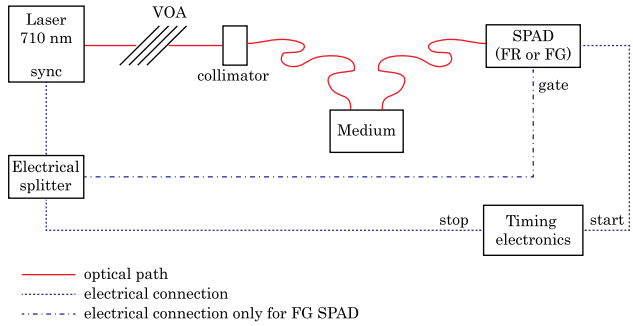

Fig. 1. Schematics of the setup: VOA, variable optical attenuator; SPAD (FR or FG), free-running SPAD or fast-gated SPAD; "timing electronics" device is a fast-gated counter or TCSPC board.

For the small ρ approach, we use a fast-gated SPAD in order to increase the dynamic range of the measurements. This is possible since the peak of early photons is rejected (by keeping the detector OFF) and then the SPAD is fast turned ON (in about 200 ps switching time) to record only late photons. For further information on this technique, see [24,25]. On the other side, for the larger interfiber distances, we use a free-running (i.e., not gated) SPAD module since the peak of early photons is lower, hence gating the time-resolved curve is not essential. Both SPADs have a diameter of the active area of 100 μm. The free-running SPAD is a commercial device (PMD series, Micro Photon Device S.r.l., Bolzano, Italy) while the fast-gated one is the custom device described in [26].

The detector provides a start signal to the timing electronics synchronous with each detected photon. Concurrently with the optical pulse, a synchronization signal is provided by the laser and is then divided into two paths.

One is used as a trigger for the gate pulse generation of the fast-gated SPAD module, while another one is provided as a stop pulse for the timing electronics (alternatively, a TCSPC board SPC 130, Becker & Hickl GmbH, Germany, or the proposed fast-gated counter).

B. Fast-gated Counter

The novel fast-gated counter provides two programmable windows whose temporal distance can be arbitrary chosen by means of the "inter-gate time" parameter (see Fig. 2). The two gates are set in the desired time position with respect to the rising edge

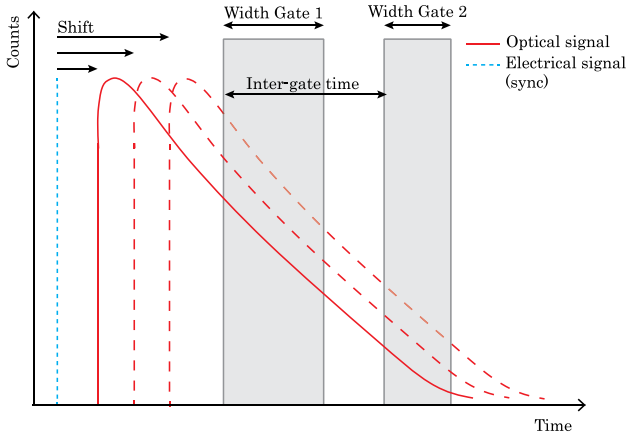

Fig. 2. Schematic representation of the proposed fast-gated counter parameters that can be changed by means of dedicated software [18]. The first pulse (blue) is the laser synchronization signal while the other curves represent various TR-curves which can be gated by means of two windows whose width and reciprocal delay can be tuned.

of the time-resolved curve by acting on the "shift" parameter. An increase of this value causes a delay in reading the avalanche pulse with respect to the sync signal. Such a delay results in a temporal shift of the whole curve toward longer times with respect to the counting windows position, as schematically depicted in Fig. 2. Each window can vary its time duration independently from the other one, in a range between 70 ps and 10 ns at 10 ps steps.

The maximum throughput achievable with the fast-gated counter is about 100 Mcps.

C. Measurements and Data Analysis

Most experimental data acquired are analyzed exploiting gating of the time-resolved curve (TR-curve). In the following, data analysis used for different kind of measurements will be detailed. All parameters set in the gated counter for the different experiments are summarized in Table 1.

1. Heterogeneous Phantom: Relative Absorption Changes

a. Contrast Measurements. In this experiment the sample consists of a calibrated liquid phantom made by a mixture of Intralipid, water, and India ink. Proportions between components are chosen to have at 710 nm an absorption coefficient (μ_a) of 0.1 cm^{-1} and a reduced scattering coefficient (μ_s') of 10 cm^{-1}.

To simulate an inhomogeneity we use totally absorbing inclusions [27] with volumes of 25 and 200 mm^3, equivalent respectively to a μ_a variation ($\Delta\mu_a$) of 0.025 cm^{-1} and 0.2 cm^{-1} over a volume of 1 cm^3. The equivalence relation between totally absorbing objects and realistic optical perturbations was exploited in [27].

The inclusion is moved in depth by means of a motorized translation stage. The position refers to the center of the inclusion, and it ranges from 2.5 mm beneath the surface of the phantom up to 50 mm deep at steps of 2.5 mm (except for the 200 mm^3 inclusion measured at 20 mm interfiber distance which ranges from 5 to 50 mm). Measurements are performed at 5 mm and then 20 mm interfiber distance using, for each case, both a TCSPC board and the fast-gated counter.

For this application we acquire counts with both timing electronics (TCSPC and the fast-gated counter) in two regions of the curve, one "early" and one "late." We choose the first gating window (early gate) delayed by 1.1 ns from the TR-curve peak in order to discard the very short travelling photons. The position of the second gating window (late gate) has to be as late as possible to record late photons but with a sufficient signal-to-noise ratio (SNR). To fulfill those conditions we use the late part of the curve where the counts are at least 10 times higher than the dark count rate. We set the inter-gate time parameter in order to open the gate windows 500 ps before this level of signal is reached.

When using the TCSPC board, the same time windows of those set in the fast-gated counter are used to compute contrast.

For both the fast-gated counter and TCSPC board, once the integral of the counts in selected gates is computed, we calculate contrast for each gate according to the following equation:

$$C = \frac{N_0 - N}{N_0}, \tag{1}$$

where N_0 is the mean number of counts acquired for the homogeneous measurements in the gate considered, while N is the number of photons detected within the same time window but when the perturbation is present.

b. Bilayer Phantom. We also tested the fast-gated counter on a bilayer phantom to see its usefulness in another application where there is no need to record the whole TR-curve.

To build a bilayer liquid phantom, a black polyvinyl chloride tank is used for this experiment [27] where two regions are created by inserting vertically a Mylar foil. On the external side, two transparent windows are present in the vertical wall. Thanks to them, it is possible to couple fibers and so to inject and collect retrodiffused photons with a reflectance geometry.

In this experiment calibrated additions of ink in the first layer (thickness is 1 cm) are done starting from $\mu_a = 0.1$ cm^{-1}. On the other side, the absorption coefficient of the second layer (5 cm thick) is kept constant and equal to 0.1 cm^{-1}. The scattering properties are kept the same for both the first and the second layer phantom ($\mu_s' = 10$ cm^{-1}). Measurements are performed only at a source detector distance of 20 mm using a free-running SPAD module.

First, we compute the $\Delta\mu_a$ exploiting both the first (early, τ_E) and second (late, τ_L) gate for each addition of ink according the following equations:

$$\Delta\mu_a^{(\tau_E)} = k_1 \ln \frac{N(\tau_E)}{N_0(\tau_E)}, \tag{2}$$

$$\Delta\mu_a^{(\tau_L)} = k_2 \ln \frac{N(\tau_L)}{N_0(\tau_L)}, \tag{3}$$

Table 1. Parameters Set on Fast-Gated Counter

	Measurements			
Parameter	Contrast (ns)	Bilayer (ns)	μ_a Assessment (ns)	*In vivo* (ns)
Delay of gate 1 with respect to TR peak	1.10	1	0.65	1.14
Gate 1 width	0.5	0.5	0.05	0.5
Inter-gate time	0.54	1.04	0.1	3.22
Gate 2 width	0.5	0.5	0.095	1.3

where N_0 is the number of counts registered when no ink is added to the top layer phantom, N represents counts registered after each addition of a calibrated quantity of ink, and k is a proportional coefficient.

We then use the method proposed in [28] to evaluate the $\Delta\mu_a$ in the deeper layer, and we compute it according the following equation:

$$\Delta\mu_a^{(\tau_L)} = -k \ln\left(\frac{N(\tau_L)}{N_0(\tau_L)} - \frac{N(\tau_E)}{N_0(\tau_E)} + 1\right). \quad (4)$$

2. *Homogeneous Phantom: Absorption Assessment*

To test the capability of the device to recover homogeneous properties just collecting photons within two time gates, we use four series (called A, B, C, and D), each one composed of eight solid phantoms made of a resin matrix of toner and TiO_2 particles [29]. Phantoms of the same series cover a range of absorption values (from 0 up to 0.38 cm^{-1} at steps of about 0.07 cm^{-1}) with a fixed reduced scattering coefficient ($\mu_s' = 5$, 7, 10.5, and 14 cm^{-1} at 710 nm for A, B, C, and D series, respectively). The nominal values of optical properties of those phantom series are used as a reference for comparison with those measured using the fast-gated counter. Mean error in optical properties assessment of the reference phantom using a broadband time-resolved diffuse spectrometer presented in [30] has been calculated around 12%.

We acquire measurements in reflectance geometry with an interfiber distance of 20 mm and using a free-running SPAD as detector.

To recover information about the absorption coefficient we use the approach proposed in [31]. We exploit the tail slope of the TR-curve where the scattering contribution is supposed to be negligible, and we express μ_a as

$$\mu_a \to -\frac{n}{c}\frac{d[R(t)]}{dt} \qquad \text{for } t \to \infty, \quad (5)$$

where $R(t)$ is the analytical expression of the TR-reflectance curve for a given interfiber distance. To compute the derivative of the TR-curve, we record the number of counts accumulated on two very close (nearly 100 ps) windows on the tail of the curve, then we calculate the differential ratio. We compute the speed of photons in the medium exploiting the refractive index (n) of resin (which is the main component of the phantom). From those simple calculations, we recover an estimation of the absorption coefficient of the measured phantom.

In order to have mostly the same SNR in both gates, we take the second window larger (95 ps) than the first one (50 ps), thus yielding nearly the same count-rate.

3. *In Vivo (Arterial Occlusion) Measurements*

We perform a proof-of-principle measurement of an arterial occlusion in the forearm of a healthy subject. The occlusion is induced with a sphygmomanometer cuff which can squeeze the forearm of the subject.

The measurement task is divided into three phases: rest (20 s), occlusion (20 s), and recovery (35 s). In the first part of the task no pressure is applied by the cuff, and the blood flow is not altered; thus a baseline condition can be recorded. After 20 s of rest, pressure applied by the cuff is rapidly increased up to 200 mm Hg in order to block circulation in both arterial and venous vessels. The same pressure is kept during the entire occlusion phase which lasts around 20 s. After that, cuff pressure is removed in order to come back to physiological conditions, and a period of recovery (35 s long) is observed. This last phase is longer than others in order to better assess how the overall hemoglobin quantity changes after occlusion removal.

Contrast here is calculated following Eq. (1) where N_0 is the mean number of counts acquired during the rest phase.

3. Results and Discussion

A. Heterogeneous Phantom: Relative Absorption Changes

The contrasts calculated using the TCSPC board and the fast-gated counter on both gates for 25 and 200 mm^3 inclusions and a source–detector distance of 20 and 5 mm are shown in Fig. 3.

For both inclusions, we see that we have higher contrast using the early gate only when the inclusion is put beneath the surface by a few millimeters. On the other hand, for deeper position of the inclusion, the late gate allows higher contrast, thus achieving a better localization of the inclusion. This behavior is in complete agreement with theory and simulations, as explained in [23].

Also the contrast profile at the two different source–detector distances is in agreement with theory. Indeed, using a short source–detector distance, the sensitivity profile allows us to detect shallow inclusions also. If the distance between source and detector is increased (e.g., 20 mm), the sensitivity profile assumes the typical "banana" shape, which is not able to probe very superficial area, thus leading to uncertainties in recovering the presence of an inclusion beneath the surface.

In all cases studied, there are no significant differences in terms of computed contrast and contrast-to-noise ratio between the TCSPC technique and fast-gated counter.

Figure 4 shows the reconstructed $\Delta\mu_a$ retrieved for a bilayer phantom holding the same scattering coefficient and an increased absorption in the first layer. The $\Delta\mu_a$ is assessed with and without applying the method proposed in [28].

In the first (top) layer (magenta line) we can see an increase in $\Delta\mu_a$ that is reflected in the second (bottom) layer if the method is not applied (dotted blue line). Conversely, if Eq. 4 is used (blue solid line), the absorption coefficient for the bottom layer does not

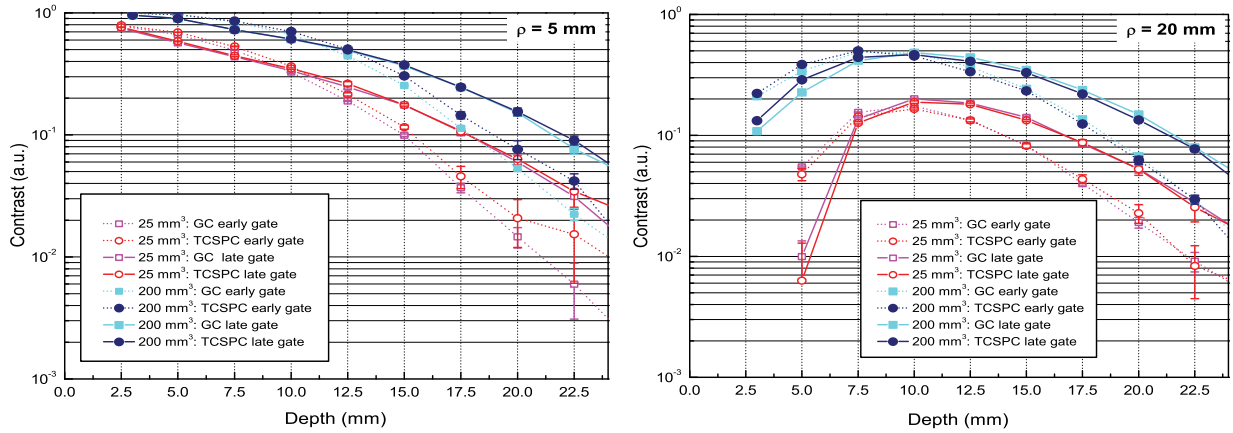

Fig. 3. Contrast calculated for 25 mm^3 (red and magenta open symbols) and 200 mm^3 (blue and cyan bold symbols) on a "late gate" (solid line) and "early gate" (dotted line) using both TCSPC board (TCSPC, circle symbol) and gated counter (GC, square symbol). Measurements are performed at 5 mm interfiber distance (left graph) and 20 mm (right graph).

present any significant change in agreement with the fact that no ink is added.

These experiments highlight the usefulness of the fast-gated counter: in these cases there is no need to record the whole TR-curve (as TCSPC does), but, with the proper algorithm, only the total number of counts in two time gates is needed. Therefore a fast-gated counter can strongly simplify and reduce costs of a typical TR setup leading to a good estimation of μ_a changes in depth occurring in a bilayer structure when absorption coefficient variations can occur also within the top layer (e.g., functional brain imaging).

In addition, high throughput (up to 100 Mcps) is another important feature of this device. It has to be compared with the maximum count-rate of 8 Mcps achievable with a TCSPC board [32]. In fact, even if detectors capable of high throughputs do exist [33–37], the conversion time of the timing electronics is limited, and not all pulses corresponding to a detected avalanche are properly converted from the TCSPC board itself. This results in a much lower throughput than the real count-rate given by the detector (e.g., at 8 Mcps count-rate, TCSPC throughput is around 4 Mcps). The higher throughput of the fast-gated counter allows us to increase the total number of photon counts for a given acquisition time with respect to a TCSPC system, thus potentially resulting in a higher SNR of the measurement.

B. Homogenous Phantom: Absorption Assessment

Eight series of calibrated solid phantoms are measured to prove the capability of the fast-gated counter to recover the absorption coefficient of a medium and also to assess the linearity of recovered μ_a values.

In Fig. 5 are shown results obtained from the data analysis explained in Section 2.C: the black line represents the expected values, while the recovered coefficients for A, B, C, and D series are shown in colors. For all measured phantoms, the standard deviation of the computed μ_a is low and not easily noticeable in graphs. We can also notice a systematic error on the accurate assessment of the absolute μ_a related to the scattering coefficient, with a general

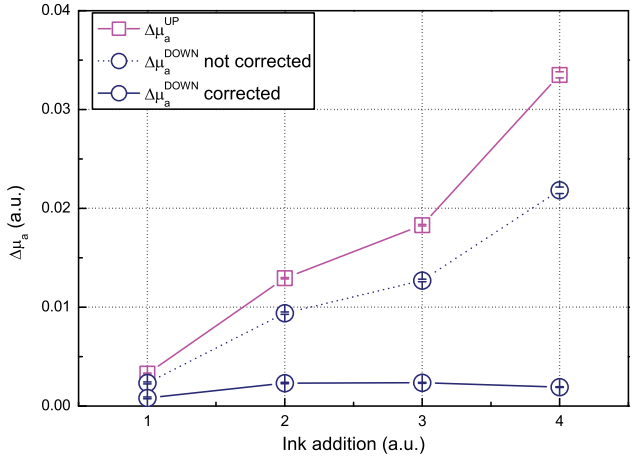

Fig. 4. Recovered changes of absorption coefficient in top layer (magenta line) and bottom one (blue line) with and without correction for early photons (respectively solid and dotted line).

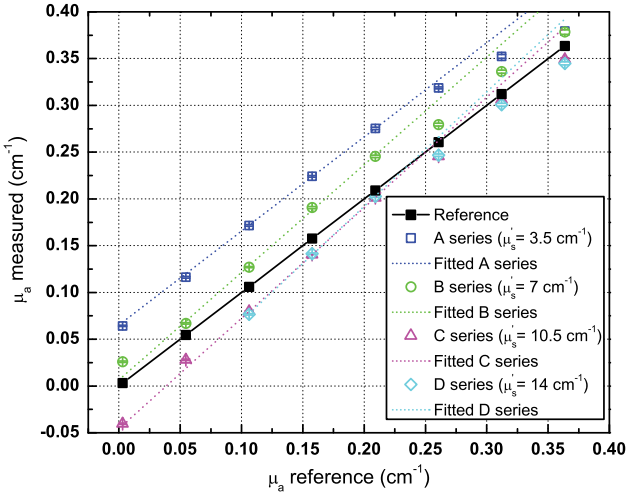

Fig. 5. Measured absorption coefficients (blue, green, magenta, and cyan lines) versus reference (black line) value for all phantom series (respectively, $\mu_s' = 3.5$, 7, 10.5, and 14 cm^{-1} at 710 nm).

underestimation for $\mu_s' > 10$ cm^{-1} and an overestimation for $\mu_s' \leq 7.5$ cm^{-1} with a mean error (computed for $\mu_a > 0.1$ cm^{-1}) of 11% for all series except for A series (mean error 20%). Such an error in the μ_a measurement is still acceptable for applications where the knowledge of optical properties is needed (e.g., breast density for cancer risk assessment).

For other applications (e.g., fruit harvesting or oximetry) the assessment of $\Delta\mu_a$ is crucial, and so the linearity of the recovered absorption coefficient is a fundamental feature. In Table 2 we report results of the linear interpolation of recovered μ_a. We exclude from the fitting process $\mu_a > 0.3$ cm^{-1} where the diffusion approximation is not perfectly valid.

The fit accuracy is very high (R^2 larger than 0.99 for all series), thus the computed values have a good linearity. The slope of the fitted curve has a value which is close to 1 with a maximum error of about 12% (for B series), thus allowing a good $\Delta\mu_a$ estimation even if the nominal value is under- or overestimated.

Looking at the intercept value of the fitted curves listed in Table 2, is possible to verify that for $\mu_s' < 10$ cm^{-1} there is an overestimation of μ_a while for $\mu_s' > 10$ cm^{-1} values are generally underestimated.

This coupling between μ_a and μ_s' is probably due partly to the inaccuracy of the approximation in Eq. (5) for finite values of t, and partly to the effect of convolution with the instrumental response function (IRF).

We can conclude that also in applications where the main goal is to quantify the relative changes of μ_a (e.g., differences between two situations: rest and task period), the fast-gated counter is suitable.

The small width provided by the fast-gated counter is one of the most interesting features of this novel device, since other commercial gated counters cannot generate windows below 1 ns [19] (in some cases 5 ns [20,21]), thus not allowing, for example, use of the approximation of Eq. (5) to compute μ_a or $\Delta\mu_a$.

However, the experimental conditions chosen for those trials are not particularly challenging, since the combination of optical properties and interfiber distance cause the time-resolved curve to be well distinguished from the IRF that could otherwise affect the exponential decay. Nonetheless, the chosen parameters are typical of a diffuse spectroscopy measurement in the 600–900 nm range on biological tissues *in vivo*.

C. *In Vivo* Measurement

Figure 6 shows the contrast recorded using the gated counter during the *in vivo* cuff-occlusion on the arm.

Table 2. Fitting Results

Phantom Series	R^2	Slope	Intercept
A	0.9987	1.00	+0.06
B	0.9930	1.04	+0.02
C	0.9973	1.12	−0.04
D	0.9930	1.11	−0.04

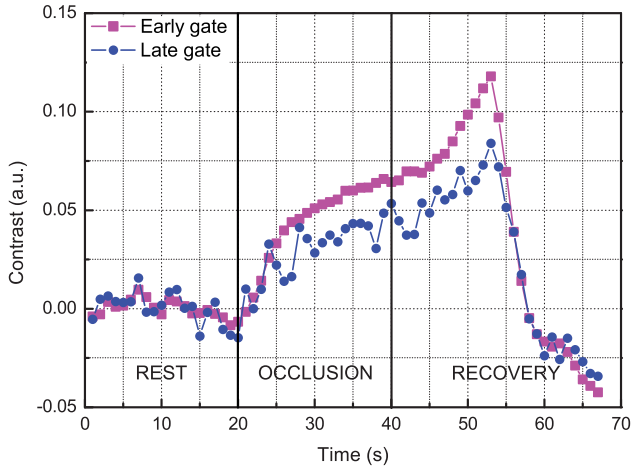

Fig. 6. Contrast computed during the arterial occlusion experiment. In magenta, photons revealed during the first gate while in blue are represented those accumulated within the second window. Lower SNR of contrast for the late gate is due to a smaller count-rate.

It is clearly noticeable that there are different task-related trends. During the rest phase, the contrast is pretty stable. On the other hand, when the occlusion starts, an increase in contrast is present and it is followed by a sudden fall some seconds after cuff release. Considering that at 710 nm there is a larger sensitivity to deoxygenated hemoglobin (due to different absorption of oxy- and deoxygenated hemoglobin, O_2Hb and HHb), the contrast trend is in agreement with literature [38]. Indeed, during the occlusion phase an increase in HHb is observed. As soon as the cuff is released, a fast overshoot of O_2Hb is recorded followed by a slow return to baseline conditions.

With this experiment we can demonstrate that using the novel fast-gated counter it is possible to monitor transients occurring during, for example, a muscle oxygenation.

4. Conclusions and Future Perspectives

In this work we proposed the use of a fast-gated counter in order to simplify the processing electronics in TR-DOS measurements where traditionally the TCSPC technique is adopted.

We first demonstrated the equivalence in term of achievable contrast between a fast-gated counter and a more expensive TCSPC board when detecting a localized optical perturbation. We then showed that using counts accumulated by the fast-gated counter during only two time gates, absorption changes in a bilayered phantom can be retrieved. Seemingly, the slope of the photon temporal distribution as recovered from the two gated counter gates is sufficient to assess the absorption coefficient of a homogeneous phantom. Finally, *in vivo* cuff-occlusion measurements on the arm were performed, enlightening the capability of the proposed fast-gated counter to properly register transients due to physiological response to an occlusion.

The limitations of the present approach could derive for particularly challenging applications, as for instance in case of very high absorptions—causing important effects of the nonideal IRF—or for scattering changes that could affect the two-gate absorption estimate. Nonetheless, in standard cases, as those presented here, the device is mostly effective.

The very high throughput of the fast-gated counter allows increasing the power injected in the sample without significant measurement distortions. Such a high throughput represents an important difference with respect to standard TCSPC devices where the maximum count-rate is also limited by the Poisson distribution. This allows increasing the power injected (within the intrinsic limits set by safety regulations for *in vivo* measurements) and so to enhance SNR or reduce measurement time with respect to other classical spectroscopy setups. The limit in the maximum achievable count-rate is now represented by the detector. The use of an array of detectors, for example, can overcome this limitation, thus enabling the use of the fast-gated counter at its best potential.

In addition the previous advantages, the use of a fast-gated counter allows reducing setup complexity, dimensions, and cost. On one hand, the TCSPC technique can provide information about the whole TR-curve, but on the other hand, for some applications there is no need to acquire the whole distribution of remitted photons. In those cases, the overall number of counts collected within two gates can be sufficient, and so a fast-gated counter can represent a valid alternative.

The fast-gated counter could be simplified even further by squeezing it onto a single application-specific integrated circuit. Once the miniaturization is done, a microcontroller can also be integrated in the same circuit as the fast-gated counter so as to perform data analysis directly on the chip. In this way, for example, calculation of $\Delta\mu_a$ (in both homogenous or bilayer phantom) or even μ_a assessment can be done without need of any computer and postprocessing analysis. Such a miniaturization, together with compact laser sources (as, for example, compact-pulsed lasers) and detectors (e.g., compact SPAD modules) would lead to a portable, on-field, real-time, and low-cost TR-DOS instrumentation.

For all those reasons, multiple and multidisciplinary fields can take advantages of this fast-gated counter as, for example, high throughput parallel imaging systems for brain monitoring or optical mammography and also for fruit harvesting analysis.

The authors wish to thank Luca Anni, Alberto Ghezzi, Stefano Moro, and Susanna Tagliabue for their help during experimental measurements and Irene Perali for her help in developing the fast-gated counter. Contribution from the EU Seven Framework Programme under the project LASERLAB EUROPE no. 284464 is gratefully acknowledged. We acknowledge nEUROPt European Project and, in particular, Fianium Ltd. for developing and making available the four-wave mixing laser source.

References

1. A. Yodh and B. Chance, "Spectroscopy and imaging with diffusing light," Phys. Today **48**(3), 34–41 (1995).
2. S. Del Bianco, F. Martelli, and G. Zaccanti, "Penetration depth of light re-emitted by a diffusive medium: theoretical and experimental investigation," Phys. Med. Biol. **47**, 4131–4144 (2002).
3. T. Durduran, R. Choe, W. B. Baker, and A. G. Yodh, "Diffuse optics for tissue monitoring and tomography," Reports Prog. Phys. **73**, 076701 (2010).
4. J. Selb, J. J. Stott, M. A. Franceschini, A. G. Sorensen, and D. A. Boas, "Improved sensitivity to cerebral hemodynamics during brain activation with a time-gated optical system: analytical model and experimental validation," J. Biomed. Opt. **10**, 011013 (2005).
5. J. Steinbrink, H. Wabnitz, H. Obrig, A. Villringer, and H. Rinneberg, "Determining changes in NIR absorption using a layered model of the human head," Phys. Med. Biol. **46**, 879–896 (2001).
6. D. Contini, L. Zucchelli, L. Spinelli, M. Caffini, R. Re, A. Pifferi, R. Cubeddu, and A. Torricelli, "Review: brain and muscle near infrared spectroscopy/imaging techniques," J. Near Infrared Spectrosc. **20**, 15–27 (2012).
7. D. Grosenick, K. T. Moesta, M. Möller, J. Mucke, H. Wabnitz, B. Gebauer, C. Stroszczynski, B. Wassermann, P. M. Schlag, and H. Rinneberg, "Time-domain scanning optical mammography: I. recording and assessment of mammograms of 154 patients," Phys. Med. Biol. **50**, 2429–2449 (2005).
8. P. Taroni, A. Torricelli, L. Spinelli, A. Pifferi, F. Arpaia, G. Danesini, and R. Cubeddu, "Time-resolved optical mammography between 637 and 985 nm: clinical study on the detection and identification of breast lesions," Phys. Med. Biol. **50**, 2469–2488 (2005).
9. T. Yates, J. C. Hebden, A. Gibson, N. Everdell, S. R. Arridge, and M. Douek, "Optical tomography of the breast using a multi-channel time-resolved imager," Phys. Med. Biol. **50**, 2503–2517 (2005).
10. X. Intes, "Time-domain optical mammography softscan: initial results 1," Acad. Radiol. **12**, 934–947 (2005).
11. Y. Ueda, K. Yoshimoto, E. Ohmae, T. Suzuki, T. Yamanaka, D. Yamashita, H. Ogura, C. Teruya, H. Nasu, E. Ima, H. Sakahara, M. Oda, and Y. Yamashita, "Time-resolved optical mammography and its preliminary clinical results," Technol. Cancer Res. Treat. **10**, 393–401 (2011).
12. P. Taroni, G. Quarto, A. Pifferi, F. Ieva, A. M. Paganoni, F. Abbate, N. Balestreri, S. Menna, E. Cassano, and R. Cubeddu, "Optical identification of subjects at high risk for developing breast cancer," J. Biomed. Opt. **18**, 060507 (2013).
13. L. Enfield, G. Cantanhede, M. Douek, V. Ramalingam, A. Purushotham, J. Hebden, and A. Gibson, "Monitoring the response to neoadjuvant hormone therapy for locally advanced breast cancer using three-dimensional time-resolved optical mammography," J. Biomed. Opt. **18**, 056012 (2013).
14. A. Pifferi, A. Torricelli, P. Taroni, A. Bassi, E. Chikoidze, E. Giambattistelli, and R. Cubeddu, "Optical biopsy of bone tissue: a step toward the diagnosis of bone pathologies," J. Biomed. Opt. **9**, 474–480 (2004).
15. A. Bellincontro, A. Taticchi, M. Servili, S. Esposto, D. Farinelli, and F. Mencarelli, "Feasible application of a portable NIR-AOTF tool for on-field prediction of phenolic compounds during the ripening of olives for oil production," J. Agric. Food Chem. **60**, 2665–2673 (2012).
16. I. Bargigia, A. Nevin, A. Farina, A. Pifferi, C. D'Andrea, M. Karlsson, P. Lundin, G. Somesfalean, and S. Svanberg, "Diffuse optical techniques applied to wood characterization," J. Near Infrared Spectrosc. **21**, 259–268 (2013).
17. J. Johansson, S. Folestad, M. Josefson, A. Sparén, C. Abrahamsson, S. Andersson-Engels, and S. Svanberg, "Time-resolved NIR/Vis spectroscopy for analysis of solids: pharmaceutical tablets," Appl. Spectrosc. **56**, 725–731 (2002).

18. G. Boso, A. Tosi, A. Dalla Mora, and F. Zappa, "High-throughput gated photon counter with two detection windows programmable down to 70 ps width," Rev. Sci. Instrum. **85**, 013107 (2014).
19. Becker & Hickl GmbH, "Datasheet," PMS-400A May 2004.
20. Stanford Research Systems, "Datasheet," SR400.
21. Agilent Technologies, "Datasheet," Agilent 53131A/132A/181A Counters (2014).
22. A. Torricelli, A. Pifferi, L. Spinelli, R. Cubeddu, F. Martelli, S. Del Bianco, and G. Zaccanti, "Time-resolved reflectance at null source–detector separation: improving contrast and resolution in diffuse optical imaging," Phys. Rev. Lett. **95**, 078101 (2005).
23. A. Pifferi, A. Torricelli, L. Spinelli, D. Contini, R. Cubeddu, F. Martelli, G. Zaccanti, A. Tosi, A. Dalla Mora, F. Zappa, and S. Cova, "Time-resolved diffuse reflectance using small source-detector separation and fast single-photon gating," Phys. Rev. Lett. **100**, 138101 (2008).
24. A. Tosi, A. Dalla Mora, F. Zappa, A. Gulinatti, D. Contini, A. Pifferi, L. Spinelli, A. Torricelli, and R. Cubeddu, "Fast-gated single-photon counting technique widens dynamic range and speeds up acquisition time in time-resolved measurements," Opt. Express **19**, 10735–10746 (2011).
25. A. Dalla Mora, A. Tosi, F. Zappa, S. Cova, D. Contini, A. Pifferi, L. Spinelli, A. Torricelli, and R. Cubeddu, "Fast-gated single-photon avalanche diode for wide dynamic range near infrared spectroscopy," Sel. Top. Quantum Electron. **16**, 1023–1030 (2010).
26. G. Boso, A. Dalla Mora, A. Della Frera, and A. Tosi, "Fast-gating of single-photon avalanche diodes with 200 ps transitions and 30 ps timing jitter," Sens. Actuator A **191**, 61–67 (2013).
27. F. Martelli, A. Pifferi, D. Contini, L. Spinelli, A. Torricelli, H. Wabnitz, R. Macdonald, A. Sassaroli, and G. Zaccanti, "Phantoms for diffuse optical imaging based on totally absorbing objects, part 1: basic concepts," J. Biomed. Opt. **18**, 066014 (2013).
28. D. Contini, L. Spinelli, A. Torricelli, A. Pifferi, and R. Cubeddu, "Novel method for depth-resolved brain functional imaging by time-domain NIRS," Proc. SPIE **6629**, 662908 (2007).
29. A. Pifferi, A. Torricelli, A. Bassi, P. Taroni, R. Cubeddu, H. Wabnitz, D. Grosenick, M. Möller, R. Macdonald, J. Swartling, T. Svensson, S. Andersson-Engels, R. L. P. van Veen, H. J. C. M. Sterenborg, J.-M. Tualle, H. L. Nghiem, S. Avrillier, M. Whelan, and H. Stamm, "Performance assessment of photon migration instruments: the MEDPHOT protocol," Appl. Opt. **44**, 2104–2114 (2005).
30. A. Pifferi, A. Torricelli, P. Taroni, D. Comelli, A. Bassi, and R. Cubeddu, "Fully automated time domain spectrometer for the absorption and scattering characterization of diffusive media," Rev. Sci. Instrum. **78**, 053103 (2007).
31. S. L. Jacques, "Time-resolved reflectance spectroscopy in turbid tissues," IEEE Trans. Biomed. Eng. **36**, 1155–1161 (1989).
32. W. Becker, *The BH TCSPC Handbook*, (Becker & Hickl GmbH, 2008).
33. Excelitas Technologies, "C30742-11 Series," http://www.excelitas.com/Downloads/DTS_C30742-11-050_Series_SiPM .pdf
34. Picoquant, "PDM series," http://www.picoquant.com/products/category/photon-counting-detectors/pdm-series-single-photon- avalanche-diodes.
35. Y. Liang, E. Wu, X. Chen, M. Ren, Y. Jian, G. Wu, and H. Zeng, "Low-timing-jitter single-photon detection using 1-GHz sinusoidally gated InGaAs/InP avalanche photodiode," IEEE Photon. Technol. Lett. **23**, 887–889 (2011).
36. A. Tosi, C. Scarcella, G. Boso, and F. Acerbi, "Gate-free InGaAs/InP single-photon detector working at up to 100 mcount/s," IEEE Photon. J. **5**, 6801308 (2013).
37. A. Korneev, P. Kouminov, V. Matvienko, G. Chulkova, K. Smirnov, B. Voronov, G. N. Gol'tsman, M. Currie, W. Lo, K. Wilsher, J. Zhang, W. Słlysz, A. Pearlman, A. Verevkin, and R. Sobolewski, "Sensitivity and gigahertz counting performance of NbN superconducting single-photon detectors," Appl. Phys. Lett. **84**, 5338–5340 (2004).
38. R. A. De Blasi, F. Safoue, and M. Ferrari, "Noninvasive measurement of human forearm oxygen consumption by near infrared spectroscopy," Eur. J. Appl. Physiol. **67**, 20–25 (1993).